A Global Non-Hydrostatic Dynamical Core Intercomparison of Idealized Squall Lines.

Nicholas Androski[1]

[1]University of Michigan, Climate and Space Sciences and Engineering

May 14, 2026

Abstract

Advances in computational power have led to the emergence of Global Storm Resolving Models (GSRMs) that leverage non-hydrostatic dynamical cores and kilometer-scale resolutions on global domains to explicitly resolve deep convective storms, such as squall lines, in contrast to the reliance on convective parameterizations in traditional Global Climate Models (GCMs). This work focuses on characterizing how the choice of dynamical core – the component of an atmospheric model that solves the equations of fluid flow – impacts the simulation of convection. We conduct this analysis with idealized, analytic squall line experiments at kilometer-scale resolutions with a reduced-radius framework. In particular, we benchmark the developmental non-hydrostatic version of the spectral element model (SE-NH) in comparison with two other GSRMs in the Community Earth System Model version 3 (CESM3): Model for Prediction Across Scales (MPAS) and Finite Volume Cubed (FV^3). We find that SE-NH captures key dynamical features in alignment with the Rotunno-Klemp-Weisman (RKW) theory of squall line development, but produces no trailing stratiform precipitation and poor anvil cloud structure. While the lack of stratiform precipitation is likely due to the simplicity of the microphysics used in the experiments, the comparison with the other GSRMs suggests that the anvil cloud structure is sensitive to the choices of numerical diffusion and turbulence closure. This proof-of-concept study demonstrates the value of idealized squall line simulations in understanding convective sensitivities within GSRMs, and future work will focus on developing a more robust set of squall line experiments that can isolate the sensitivities of the dynamical core from the sensitivities of the parameterized physics.

1 Introduction

As global climate models (GCMs) reach horizontal resolutions that resolve convective storm systems, it becomes more critical to determine how convection is sensitive to various modeling decisions. This study primarily aims to understand, at a process level, how the choice of the dynamical core – the component of a GCM that solves the resolved equations of fluid flow – impacts convection among GCMs at kilometer-scale (km-scale) spatial resolutions. Since the development of the first climate models, one of the principle questions in the field is to understand the sensitivity of the climate to an increase in greenhouse gas concentration. This sensitivity depends on a complex network of feedback processes that act to either amplify or reduce the warming effect. The predicted change in global-mean surface temperature to a doubling of CO_2, the Equilibrium Climate Sensitivity (ECS), is a common metric to measure greenhouse gas influence. While the understanding of feedback mechanisms has improved significantly, the spread among GCMs in the ECS remains large. In the state-of-the-art Coupled Model Intercomparison Project 6 (CMIP6), the ECS lies between $1.83°C$ to $5.67°C$, an increase from the previous CMIP5 generation of models [Chen *et al.* 2021; Scafetta 2022]. The radiative feedbacks from clouds contribute the largest uncertainty in the intermodel spread [Ceppi *et al.* 2017; Schär *et al.* 2020]. It is thought that the large spread occurs because clouds are determined by small-scale processes – such as convection, turbulence, and microphysics – which are often unresolved at the typical 50 to 100 km grid spacing of GCMs and must be parameterized. Parameterization uses the resolved, large-scale variables to estimate the collective effects of the unresolved, small-scale processes.

The continuing growth of computational capacity has enabled the simulation of the atmospheric general circulation on non-hydrostatic, km-scale domains that can begin to explicitly resolve convection [Satoh *et al.* 2019]. On the scale of synoptic circulations, the atmosphere to a good approximation is in hydrostatic balance whereby the force of gravity is in balance with the vertical pressure gradient force. This assumption is often baked in to the formulation of GCMs. However, at the km-scale, deviations from the hydrostatic balance can arise due to convection, the vertical – often turbulent – transport of moisture and heat induced by buoyancy. The representation of convection requires the inclusion of non-hydrostatic terms in the equations of motion. It is thought that global, non-hydrostatic, km-scale models, commonly referred to as Global Storm Resolving Models (GSRMs), can reduce the uncertainty in cloud feedback and improve the understanding of how clouds impact the larger scale circulation by explicitly representing convection, rather than a parameterization. In particular, the km-scale can explicitly represent the dynamics and structure of mesoscale convective systems (MCSs), defined as organized collections of cumulonimbus thunderstorms with precipitation scales of at least 100 km in length [Houze Jr. 2004]. MCSs are a large contributor to precipitation within the tropics and midlatitudes [Haberlie & Ashley 2019] and are a major cause of hazardous weather – such as floods, hail, tornadoes, and strong wind storms called derechos. Furthermore, they serve as an important link between convection and the larger-scale circulation. They facilitate the Madden Julian Oscillation, the dominant mode of tropical intraseasonal variability [C. Zhang 2005], and influence large-scale baroclinic wave activity in the midlatitudes.

As a first step toward multi-decadal global km-scale simulations, prototype GSRM simulations have been made on seasonal time scales. Most notably, the DYnamics of the Atmospheric general circulation Modeled On Non-hydrostatic Domains (DYAMOND) intercomparison project has compared GSRMs at resolutions of 5 km or less [Satoh *et al.* 2019; Stevens *et al.* 2019]. These global simulations and decadal km-scale regional models demonstrate that modeling at the km-scale provides significant improvement in the diurnal timing and intensity of precipitation, the frequency and intensity of hourly heavy precipitation, and vertical cloud structure [Ban *et al.* 2014; Berthou *et al.* 2020; Feng *et al.* 2023; Kendon *et al.* 2012; Prein, Langhans, *et al.* 2015; Prein, Wang, *et al.* 2025]. However, many challenges remain, as convection is generally too strong and less organized among GSRMs due to an excess in small scale variability [Freischem *et al.* 2024]. GSRMs tend to produce updrafts that are too wide and intense [Prein, Wang, *et al.* 2025], underestimate stratiform rain [Feng *et al.* 2023], and produce a higher frequency of hourly convective precipitation at the grid point level compared to observations – often referred as the "popcorn" convection problem [Caldwell *et al.* 2021; Freischem *et al.* 2024]. Feng *et al.* 2023 suggest that insufficient entrainment mixing in updrafts and sensitivities to ice microphysical processes are consistent with observed deficiencies. In addition, at the km-scale, convection is only partially resolved, lying at a "gray-zone" of turbulent motions where horizontal grid spacing is similar in scale to energy-containing eddies [Bryan, Wyngaard, *et al.* 2003; Wyngaard 2004]. Several studies indicate that while bulk convergence of storm-averaged quantities with resolution occurs at the km-scales, structural convergence of individual convective cells does not occur until scales on the order of 100 meters or smaller where the energy containing eddies are resolved [Bryan, Wyngaard, *et al.* 2003; Prein, Wang, *et al.* 2025]. In this gray-zone, the representation of turbulent and microphysical processes – still unresolved at the km-scale – are essential.

The development of "scale-aware" parameterizations designed to handle the gray-zone is an active area of research, but global km-scale simulations face several bottlenecks that have made the progress slow. They remain extremely expensive to run, face a gap in leveraging the newest generation of computational architectures (the software productivity gap; see Lawrence *et al.* 2018), and produce an avalanche of data on the scale of terabytes to petabytes that makes the processing and tuning of GSRMs considerably challenging [Schär *et al.* 2020]. There is a critical need for efficient techniques that can probe model sensitivities and reassess the assumptions used in physics parameterizations at the km-scale through process-based understanding.

The simulation of squall lines – a type of linearly-organized MCS – using analytic initial conditions and simplified parameterizations of microphysical and turbulent processes are an effective tool to expose sensitivities due to differences between dynamical cores and physics-dynamics coupling in the simulation of convection. Whereas the dynamical core is the component of an atmospheric model that solves the resolved equations of fluid motion, the physics refers to the subgrid, unresolved, processes that must be parameterized. Differences in dynamical cores reflect different representations of the same physical processes and are a key component in understanding uncertainty in large-scale climate change projections and MCS characteristics observed in GSRMs. Physics-dynamics coupling, i.e. the treatment in how the compartmentalized physics and dynamics components are combined, can also dominate and determine the overall model error even as the error associated with the individual components decreases [Donahue & Caldwell 2018; Gross *et al.* 2018]. While the sensitivities of numerical squall line simulations to the subgrid turbulence parameterization [Lai & Waite 2020; Moeng *et al.* 2010; Takemi & Rotunno 2003], microphysics [Bryan & Morrison 2012], horizontal resolution [Bryan, Wyngaard, *et al.* 2003; Weisman, Skamarock, *et al.* 1997], vertical resolution [Lebo & Morrison 2015], and the large-scale environment [Morrison, Morales, *et al.* 2015; Potvin & Flora 2015] have been well studied, there is comparatively little information on the sensitivity to dynamical core, particularly those designed for global, spherical domains, where convection has traditionally been parameterized.

Within the Numerical Weather Prediction (NWP) community, idealized squall line experiments are frequently used as a benchmark for comparing the representation of non-hydrostatic convective motions. Bryan, Knievel, *et al.* 2006 evaluate several finite-difference, non-hydrostatic models typically used in NWP and found that the models captured the overall squall line structure. However, their simulations displayed systematic differences that could be traced back to numerical choices within the dynamical core related to the schemes for advection and vertical diffusion. Recently, Lou Wicker [manuscript in review for Mon. Wea. Rev.] used idealized squall line simulations to isolate precipitation biases in weakly sheared environments observed in NOAA's Rapid Refresh Forecast System (RRFS) and identified a difference in the numerical implementation of the vertical non-hydrostatic equations compared to other NWP models that caused the production of excessively strong updrafts. In the Dynamical Core Model Intercomparison Project 2016 (DCMIP 2016), the simulation of a supercell on a reduced radius framework, based upon the work of Klemp, Skamarock & Park 2015, is used to compare 10 non-hydrostatic global models. The study reveals systematic differences caused by a combination of numerical discretization, physics-dynamics coupling, and numerical diffusion choices.

This paper expands on the intercomparison of convective, non-hydrostatic dynamics in DCMIP 2016 through the evaluation of three global non-hydrostatic dynamical cores in the National Center for Atmospheric Research (NCAR) Community Earth System Model 3 (CESM3) using idealized squall line simulations. In particular, we focus on the developmental non-hydrostatic version of the spectral element dynamical core (SE-NH) imported from the U.S. Department of Energy via the NSF-funded Storm-resolving SPEctral Element Dycore (StormSPEED) project. The development of the spectral element model has primarily focused on the accurate representation of the global climate, and so a key objective of this work is to understand how the SE-NH model simulates mesoscale processes that have traditionally been parameterized. As a first step in this intercomparison, we seek to address two objectives. First, to assess the ability of SE-NH to simulate the dynamical structure of a squall line across several different resolutions within the km-scale through the lens of Rotunno-Klemp-Weisman (RKW) Theory [Weisman & Rotunno 2004]. Second, to evaluate how the convection simulated in SE-NH compares to the two other non-hydrostatic dynamical cores in the CESM3 framework, NCAR's Model for Prediction Across Scales (MPAS) and NOAA's Finite Volume Cubed (FV^3) model, with a focus on sensitivities to different choices of diffusion. In Section 2, we outline the key design differences across the three dynamical cores and describe the squall line test configuration. In Section 3, the results of the SE-NH simulations are evaluated through the lens of RKW theory and then compared against MPAS and FV^3. Finally, Section 4 summarizes the key findings and outlines the remaining work needed to establish more robust results.

2 Methods

2.1 Dynamical Core and Physics Coupling Overview

2.1.1 Dynamical Cores

Model intercomparisons will include the three compressible, non-hydrostatic (NH) dynamical cores in the atmosphere component of CESM3, the Community Atmosphere Model version 7 (CAM7). The first is SE-NH, the non-hydrostatic E3SM spectral element dynamical core from the U.S. Department of Energy in CAM7 via the StormSPEED project [J. Dennis *et al.* 2005; J. M. Dennis *et al.* 2012; Donahue, Caldwell, *et al.* 2024; Taylor *et al.* 2020]. The second is the Finite Volume Cubed (FV^3) model developed by NOAA's Geophysical Fluid Dynamics Lab (GFDL) [Lin 2004; Putman & Lin 2007]. The third, is NCAR's Model for Prediction Across Scales (MPAS) [Klemp, Skamarock & Dudhia 2007; Ringler *et al.* 2010; Skamarock *et al.* 2012; Thuburn *et al.* 2009]. Key design choices of the numerical schemes employed by each model are highlighted in Table 1. For a thorough description of general design choices in NH dynamical cores see Ullrich *et al.* 2017 which includes an overview of ACME (a prior name for E3SM), FV^3, and MPAS.

In CAM, which computes physics within each atmospheric column, horizontal numerical and physical mixing is done by the dynamical core. Numerical mixing is important for removing the build-up of energy at the grid-scale due to mechanisms such as artificial grid-scale noise from the numerical scheme or the lack of physical dissipation processes that occur below the grid-scale. Hyperviscosity approaches are popular because they are easily tunable and scale-selective, avoiding excessive diffusion of the large-scale, resolved features of atmospheric flow. Numerical mixing can also be introduced by monotonic limiters used in the horizontal advection schemes or in the remapping of vertical Lagrangian levels onto reference Eulerian levels in models with floating vertical coordinates like SE-NH and FV^3. Physical mixing refers to diffusion schemes for subgrid turbulent fluxes that become important at the km-scale. A common approach is an eddy viscosity model which represents small-eddy turbulence as a dissipative mechanism that transfers energy from resolved to subgrid scales, and is appropriate for Large Eddy Simulations (LES) where the largest energy-containing eddies are resolved [Bryan, Wyngaard, *et al.* 2003]. However, at the km-scale there is less consensus on how physical mixing should be represented as energy-containing

Model	SE-NH	FV^3	MPAS
Horizontal grid	equiangular cubed-sphere	equidistant cubed-sphere	Centroidal Voronoi mesh
Horizontal staggering	A grid	C-D grid	C grid
Vertical staggering	Lorenz	Co-located	Lorenz
Vertical coordinate	Floating mass-based	Floating mass-based	Geometric height-based
Numerical method	Spectral Element	Finite Volume	Finite Volume
Temporal discretization	HEVI-IMEX	split-explicit	split-explicit

Table 1: Key design choices for the compressible, non-hydrostatic dynamical cores within CESM3: SE-NH, FV^3, and MPAS. HEVI-IMEX refers to a Horizontal Explicit Vertically Implicit (HEVI) IMplicit-EXplicit (IMEX) time stepping algorithm [Taylor *et al.* 2020] used to include fast acoustic modes with a less strict time step constraint compared to the split-explicit approaches used in FV^3 [Lin 2004] and MPAS [Klemp, Skamarock & Dudhia 2007].

eddies are only partially resolved and the transfer of energy from smaller to larger scales can be relevant.

SE-NH has two main sources of numerical diffusion: a tunable fourth-order horizontal hyperviscosity scheme and vertical dissipation from the conservative, monotone vertical remap algorithm [Taylor *et al.* 2020]. There are currently no implemented physical mixing schemes within SE-NH. MPAS also primarily uses fourth-order horizontal hyperviscosity filters for numerical mixing, but includes several options for physical second-order eddy viscosity mixing schemes. Fixed values can be used for both second-order horizontal and vertical eddy viscosity mixing. Additionally, a variant of the second-order horizontal mixing from Smagorinsky 1963 that spatially and temporally varies based on horizontal flow deformation is included. FV^3 controls numerical noise implicitly through monotonic horizontal advection schemes and explicitly by applying hyperviscosity to the damping of vorticity and divergence. Several horizontal advection options are available that range from effectively inviscid to monotonic schemes which are more diffusive. The divergence damping can be fourth-, sixth-, or eighth-order and the vorticity damping fourth- or sixth-order. The higher orders allow for more scale-selective diffusion. A flow-dependent second-order damping can be added as well, with a varying coefficient determined by vorticity and divergence instead of horizontal deformation.

2.1.2 CAM Physics-Dynamics Coupling

While the standalone version of each dynamical core have its own associated subgrid physics parameterization suite, each is coupled to CAM physics within CESM. CAM is primarily designed as a hydrostatic Earth System Model. While NH dynamical core options have recently been implemented, the physics scheme coupling continues to rely on hydrostatic assumptions to convert the model state to the input state for physics. The assumptions result in a source of bias when converting non-hydrostatic dynamics variables to hydrostatic physics variables.

CAM generally follows a sequential update split approach for physics-dynamics coupling where the physics updates the state and the dynamics updates from this state in a sequential manner. However, MPAS and SE-NH by default use a hybrid sequential splitting (HSS) approach, described

Table 2: Physical Constants.

Parameter	Definition	Value
a	Earth's radius	6.37122×10^6 m
g	Gravitational acceleration of the Earth	9.80616 m s^{-2}
c_p	Specific heat capacity at constant pressure for dry air	1004.64 J kg $^{-1}$ K^{-1}
R_d	Ideal gas constant for dry air	287.04 J kg^{-1} K^{-1}
M_v	Molar mass of dry air to water vapor ratio	0.608
p_0	Reference pressure	100,000 Pa

in detail by K. Zhang *et al.* 2018 and Donahue & Caldwell 2020. In brief, the approach – often referred to as dribbling – computes physics tendencies at the coarsest physics time step and applies them incrementally during the subcycling of dynamics (in the case of MPAS) or vertical remap steps (for SE-NH). FV^3, within CAM, uses the more traditional sequential update split approach without any dribbling.

2.2 Squall Line Test Case Description

The squall line test case, which is used to test the sensitivity of convective dynamics to dynamical core choice, is an extension of the non-rotating, reduced-radius supercell test case presented in Klemp, Skamarock & Park 2015 and applied in DCMIP 2016 [Zarzycki *et al.* 2019]. The reduced-radius technique can achieve kilometer scale resolutions on a global, spherical domain at a low computational cost, as opposed to the expense required to run GSRMs on full size Earth simulations. In this study we use a reduction factor (X) of 60, which scales the radius of the Earth by a factor $1/60$. At this scale, a spherical, quasi-uniform 1° mesh corresponds to about two kilometers of physical spacing. Klemp, Skamarock & Park 2015 demonstrated that at an even larger scale factor of $X = 120$, there was good agreement between the supercell results on a reduced-radius Earth and those on a flat Cartesian plane.

The analytic environmental background in the test case has its roots in the initialization first presented in Klemp & Wilhelmson 1978b and Weisman & Klemp 1982. It is commonly used by Rotunno, Weisman, and Klemp (RKW) in numerical squall-line experiments to represent the thermodynamic conditions of severe, mid-latitude squall lines. Their work demonstrated that the initial conditions can produce a variety of convective storm environments primarily by modifying the vertical shear profile (z_s, U_s) or the low level moisture $(q_{0,\max})$, which determines the overall convective instability. When a strong, deep vertical shear is prescribed, Klemp & Wilhelmson 1978a observed storms with strong cells with supercellular characteristics, that can split and form strong rotational updrafts. Bryan, Knievel, *et al.* 2006 observed weaker shear environments produce smaller, weaker cells spread over a broader region.

Zarzycki *et al.* 2019 provides a detailed overview of the background initial conditions and the numerical implementation used in this study. Below, we specify the modifications made to provide a more consistent initialization of squall line development suitable for intercomparison across dynamical cores. Then we discuss the specific configuration used for the experiments in this study. The physical constants and test case parameters are listed in Tables 2 and 3 respectively.

Table 3: Squall line test case parameter definitions and values.

Parameter	Definition	Value
X	Reduced Earth scaling factor	60
r_{earth}	Reduced Earth radius $(X^{-1} \cdot a)$	106187 m
θ_{trop}	Potential Temperature at the tropopause	343 K
θ_0	Temperature at the equatorial surface	300 K
T_{trop}	Temperature at the tropopause	213 K
z_{trop}	Altitude of the tropopause	12000 m
$q_{0,max}$	Maximum tropopause specific humidity	14.0 g/kg
U_s	Wind shear velocity	6, 12, 18 m s^{-1}
U_c	Coordinate frame reference velocity	5 m/s^{-1}
z_s	Shear layer top height	2500 m
Δz_U	Smooth velocity transition halfwidth	1000 m
$\Delta\theta$	Thermal perturbation magnitude	3 K
r_h	Thermal perturbation East-West horizontal halfwidth	15000 m
Δs	Thermal perturbation North-South horizontal halfwidth	60000 m
r_z	Thermal perturbation vertical halfwidth	1500 m
λ_c	perturbation center longitude	180°
ϕ_c	perturbation center latitude	0°
z_c	perturbation center altitude	1500 m

2.2.1 Test Case Modifications

The key environmental conditions for a squall line are the vertical wind shear and the convective instability. Convective instability is commonly measured by the convectively available potential energy (CAPE) which provides an upper limit on the amount of positive buoyancy for a given profile of temperature and moisture. The zonally symmetric atmospheric background state is designed to have high CAPE (~ 2415.0 J/kg) and strong low-level shear. At the surface, a free-slip boundary condition is applied. Rotation is not included as over the short time scales it is expected to have only a small effect. Simulations in the literature demonstrate that experiments with and without Coriolis effects had negligible influence on results over 6 hour time scales [Weisman, Skamarock, *et al.* 1997]. Since there is no rotation, the initial background is set up to satisfy a hydrostatic, cyclostrophic balance.

The meridional and vertical winds are initially set to zero, while the zonal wind adheres to solid body rotation of the form $u(z,\phi) = u_{\text{eq}}(z)\cos(\phi)$ where $u_{\text{eq}}(z)$ is given by

$$u_{\text{eq}}(z) = \begin{cases} U_s \frac{z}{z_s} - U_c & z < z_s - \Delta z_U \quad \text{(linear)} \\ \left(A + B\frac{z}{z_s} + C\left(\frac{z}{z_s}\right)^2\right) U_s - U_c & |z - z_s| \leq \Delta z_U \quad \text{(transition)} \\ U_s - U_c & z > z_s + \Delta z_U \quad \text{(constant)} \end{cases} \tag{1}$$

where A, B, and C produce a smooth and continuous transition between the low-level linear shear and constant wind aloft:

$$A = -\frac{z_s}{4\Delta z_U}$$
$$B = \frac{1}{2}\left(1 + \frac{z_s}{\Delta z_U}\right)$$
$$C = \frac{1}{2} - \frac{1}{4}\frac{z_s}{\Delta z_U} - \frac{1}{4}\frac{\Delta z_U}{z_s}$$

This generalizes the smooth profile in the supercell test case for arbitrary shear depth, z_s, and transition layer depth, Δz_U.

A warm potential temperature perturbation is applied near the surface to trigger convection in the unstable environment. The perturbation is most similar to a physical diabatic heating mechanism that produces a positively buoyant parcel of air. In the supercell test case, a single bubble-shaped perturbation with a 10 km horizontal radius and a 1.5 km vertical radius is included. However, this perturbation is prone to sampling variability across dynamical cores, dependent on the model resolution and the grid type. To minimize the effect of initial condition sampling biases, a cylindrical shaped perturbation is used. The cylindrical shape is oriented along the latitudinal direction and has the same longitudinal and vertical cross section. Analytically, the cylinder shape is described by

$$\theta'(\lambda,\phi,z) = \begin{cases} \Delta\theta\cos^2\left(\frac{\pi}{2}R\right) & R < 1 \text{ and } |\phi| \le \phi_{\max} \\ 0 & \text{otherwise.} \end{cases} \tag{2}$$

where $R = R(\lambda,\phi,z;\lambda_c,\phi_c,z_c)$ defines the radius from longitude λ_c and center height z_c at a given latitude

$$R(\lambda,\phi,z;\lambda_c,\phi_c,z_c) = \sqrt{\left(\frac{(\lambda-\lambda_c)r_{\text{earth}}\cos(\phi)}{r_h}\right)^2 + \left(\frac{z-z_c}{r_z}\right)^2} \tag{3}$$

and $\phi_{\max} = a\Delta s/X$ where Δs is the horizontal half width of the cylinder in the latitudinal direction. The test case parameters r_h and r_z determine the physical longitudinal and vertical radius of the cylinder. For our experiments, we use a cylinder with magnitude $\Delta\theta = 3$ K and half widths $\Delta s = 60$ km, $r_h = 15$ km, and $r_z = 1.5$ km shown in Figure 1. As mentioned by Klemp, Skamarock & Park 2015 and Zarzycki *et al.* 2019, an additional step is required to bring the perturbation into hydrostatic balance, otherwise the initial conditions are initially non-hydrostatic and create an initial adjustment period that produces large vertical velocities and noisy pressure fields [Bannon 1995]. Additionally, it is common for Earth system models, like CESM, to assume analytic initial conditions are hydrostatically balanced and make use of this assumption when initializing model variables. In Zarzycki *et al.* 2019, this additional step was not taken, and it led to bubble perturbations with varying magnitude between dynamical cores at the same resolution, on order of 0.1 K. To achieve a more consistent initialization, a hydrostatically balanced Exner perturbation, $\Pi'(z)$, is computed by an integration of the equation

$$\frac{\partial\Pi'}{\partial z} = \frac{g}{c_p\overline{\theta}_v}\left(1 - \frac{\overline{\theta}}{\theta}\right) \tag{4}$$

in each column under the boundary condition $\Pi'(0) = 0$ where $\theta = \overline{\theta} + \theta'$ is the total potential temperature. Here, the background atmospheric state, is represented with $(\overline{\ })$ quantities, and the

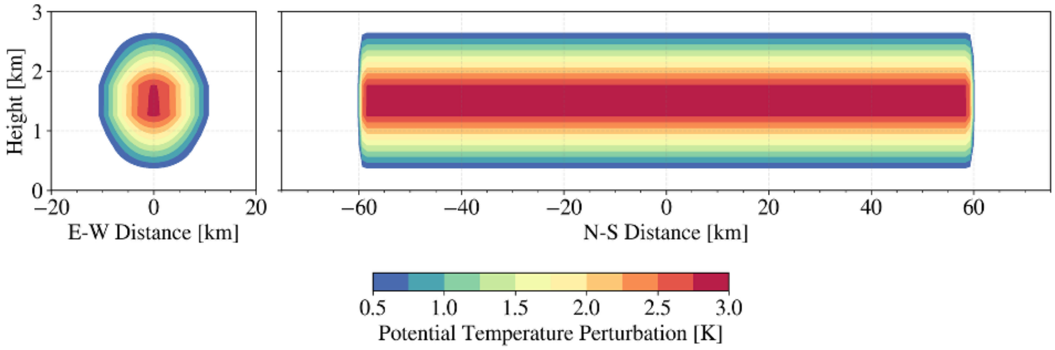

Figure 1: Cross sections of the potential temperature perturbation, θ', along the east-west direction (left) and along the north-south direction (right). The cross sections are computed from SE-NH output at $\Delta x = 1$ km.

perturbation, is represented with $(\ ')$. If Π' satisfies the above equation, then the total Exner pressure, $\Pi = \overline{\Pi} + \Pi'$, is given by

$$\frac{\partial \Pi}{\partial z} = \frac{g}{c_p \theta_v} \tag{5}$$

and is thus hydrostatically balanced. The perturbation state entails an analytically defined potential temperature perturbation θ' and an Exner pressure perturbation Π' computed such that the total Exner pressure is balanced. Moisture and winds are left unperturbed. The resulting pressure, temperature, and density perturbations along a horizontal, east-to-west, slice associated with the resulting profiles are depicted in Figure 2 for reference. Notably, the balancing step introduces perturbations above the cylinder, producing a profile that is slightly hotter (Figure 2d) and more dense (Figure 2f) aloft compared to the background.

2.2.2 Test Configuration

A reduced-radius sphere of $X = 60$ provides enough space on the sphere for the horizontal growth of the squall line over the 6 hour simulation time. Higher values of scale factors are preferable as it provides finer physical resolution, but this comes at the cost of a smaller total domain. Three horizontal resolutions, $\Delta x = 1, 2, 4$ km are considered to evaluate the sensitivity of squall-line structure across the gray-zone. All simulations use a physics time step of $\Delta t = 12$ s with sub-cycling of tracer transport and dynamics based on the default splitting specified by each model.

For each experiment we use a vertical zonal wind profile with low-level, moderate unidirectional shear ($U_s = 12$ m/s from the surface to $z_s = 2.5$ km above ground level; Figure 3a) that transitions to a constant speed aloft. We denote this shear environment as S12. For each profile, the specific humidity near the surface is held at a maximum value, $q_{0,\max}$, to represent a well-mixed boundary layer. A value of $q_{0,\max} = 14$ g/kg is specified to produce a surface-based CAPE of 1950 J/kg and a most-unstable-based CAPE (MU-CAPE) of 2415 J/kg at the equator (Figure 3b). While this study uses only a single profile of environmental instability, varying $q_{0,\max}$ can directly influence the CAPE of the background and provides another parameter to explore squall line structure.

In the vertical, all simulations have a model top of 30 km with a uniform spacing of $\Delta z = 500$ m. In the top 10 km, a Rayleigh damping layer is applied implicitly to horizontal velocities to minimize

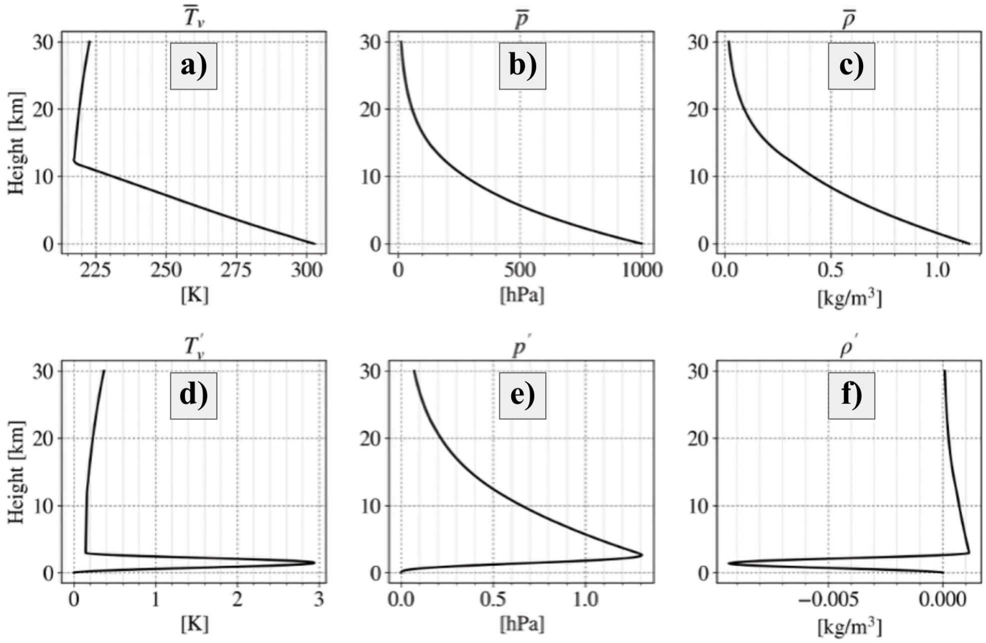

Figure 2: Equatorial vertical cross sections of temperature, pressure, and density for the background (a,b,c) and perturbation (d,e,f) of the hydrostatically balanced cylinder θ' perturbation at the center of the cylinder, (λ_c, ϕ_c).

wave reflections along the model top. A damping time-scale of $\tau = 15$ s is found to be sufficient. Each model has little qualitative sensitivity to both Rayleigh sponge strength and depth. A constant vertical and temporal resolution are used for each horizontal resolution to isolate the horizontal grid-spacing sensitivity.

The only physics parameterization in this experiment is a simple microphysics scheme. Radiative, rotational, and surface effects are unaccounted for. While studies have demonstrated the sensitivity of horizontal resolution in the representation of squall-lines, the schemes to approximate the microphysics and turbulent processes are also influential on storm intensity and structure. Studies have shown that microphysics can have particular influence on the representation of trailing stratiform precipitation and the strength of the cold pool through condensate loading, latent energy processes, and hydrometeor fall speed. However, overall storm circulation is qualitatively similar among different microphysics schemes [Bryan & Morrison 2012; Morrison, Thompson, *et al.* 2009; Morrison, Morales, *et al.* 2015]. For this test-case, we use a simple, Kessler-type one-moment bulk scheme from Klemp, Skamarock & Park 2015 that prognoses the mixing ratios of water vapor (q_v), cloud liquid (q_c), and rainwater (q_r). It effectively models warm rain processes but will miss the ice-phase processes important in the formation of trailing stratiform precipitation in midlatitudinal squall lines.

For this study, the goal is to assess the variability between the dynamical core response within the km-scale. We opt not to unify the physical and numerical mixing mechanisms across dynamical cores, instead leaving diffusion as a modeling choice to be compared. For SE-NH experiments, no turbulence closure is applied and for numerical mixing we apply the fourth-order hyperviscosity filter using the CAM-default constant coefficient used for one-degree experiments scaled by X^{-3} to account for the reduced-radius. For MPAS, the Smagorinsky turbulence closure is used along with

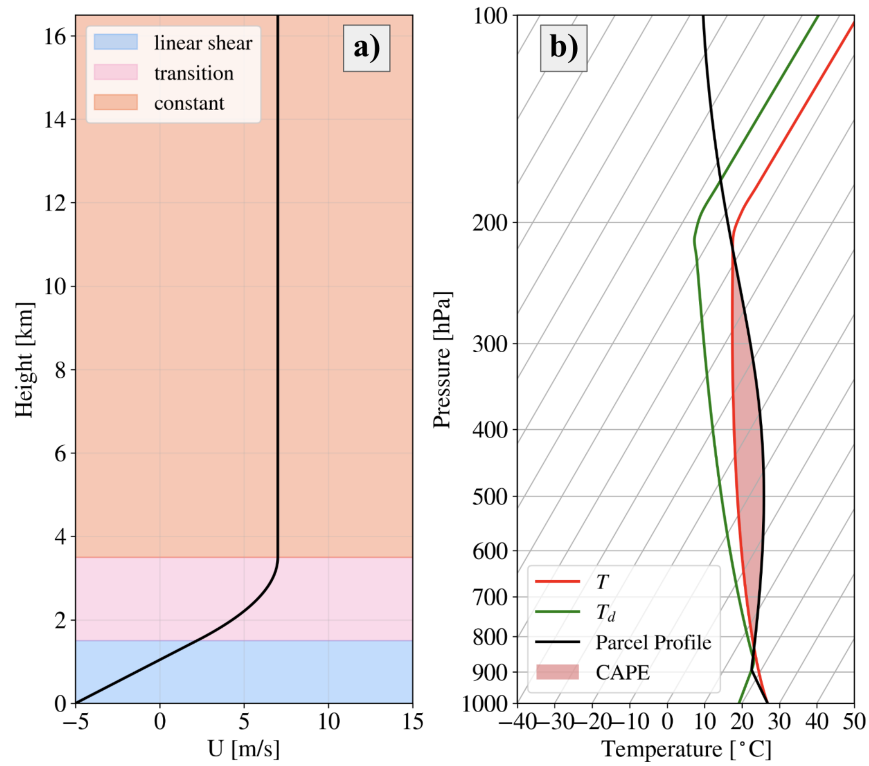

Figure 3: Background zonal wind (U) profile (a) with 12 m/s vertical shear in the first 2.5 km. Skew-T diagram (b) including the temperature (T; red), dewpoint temperature (T_d; green), and the profile of an pseudo-adiabatically lifted parcel at the surface (black) with convective available potential energy (CAPE) shaded. For $q_{0,\max} = 14.0$ g/kg, CAPE ≈ 1950 J/kg from a parcel at the surface (shaded) and ≈ 2415 J/kg from the most unstable parcel path in the profile.

a weaker fourth-order hyperviscosity filter for numerical mixing. For FV^3, diffusive monotonic options are used for advection along with sixth-order divergence damping. No turbulence closure is applied in FV^3. An additional FV^3-RRFS experiment is conducted using diffusion settings applied in NOAA's Rapid Refresh Forecast System (RRFS). RRFS is configured with minimally diffusive advection options, eighth-order divergence damping, and a flow-dependent second-order divergence damping scheme described in Section 2.1.

3 Results

3.1 Squall Line Structure in SE-NH

Across each resolution in SE-NH, the convective rise of the buoyant potential temperature perturbation triggers the development of strong updrafts that produce intense precipitation. The evaporative cooling from the rainfall induces a near surface outflow and the development of a cold pool below the updraft with potential temperature values as much as 8 K cooler than the surrounding environment. On the downshear side of the cold pool (the direction following the direction of wind shear), the outflow balances the low-level vertical wind shear to produce new, deep lifting at the

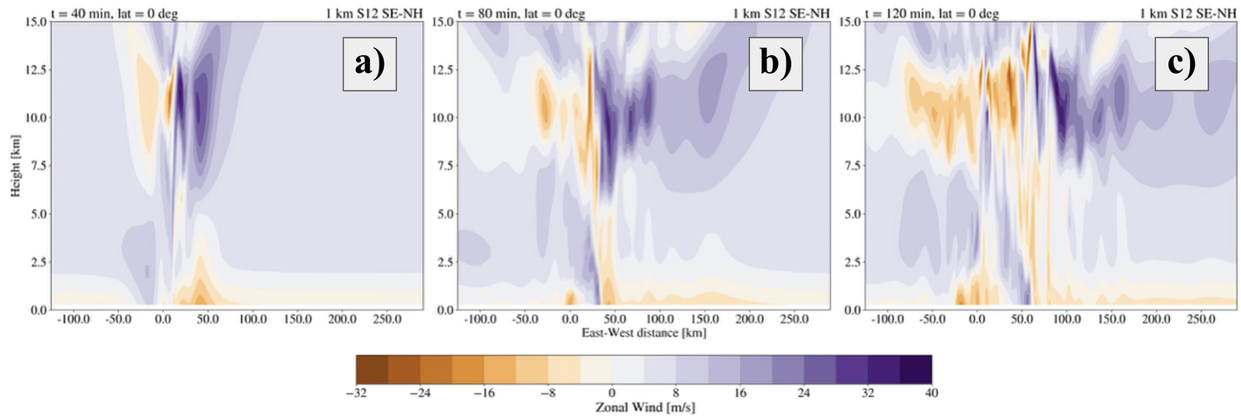

Figure 4: Equatorial vertical cross sections of zonal wind (U) for the SE-NH $\Delta x = 1$ km, S12 experiment at 40 (a), 80 (b), and 120 (c) minutes. Longitude is scaled to physical distance at the equator on the $X = 60$ reduced-radius sphere.

leading edge as described by RKW cold-pool–shear interaction theory. RKW theory is concerned with the interaction between the cold pool and the environmental wind shear, and argues that these two properties primarily govern the structure of squall lines. They suggest a squall line transitions between three stages (summarized conceptually in Figure 2 of Weisman & Rotunno 2004) where the updraft of the system tilts downshear when the cold pool intensity is weak and still developing, then tilts upright when the system reaches an optimal state where the cold pool intensity balances the shear, and finally tilts upshear (opposite of wind shear) as the cold pool intensity becomes more intense than the low level shear. The third stage, where the cold pool dominates, produces a circulation structure that is typical of mature, trailing-stratiform squall lines [Houze Jr. 2004]. The structure is characterized by the gust front, a region of strong surface winds directly below the leading edge of the cold pool where new convective cells are being generated. The cold pool drives an ascending front-to-rear inflow that feeds new convection. The resulting precipitation strengthens the cold pool and drives the development of a descending rear inflow of air. The vertical cross section of the zonal wind at the equator for the $\Delta x = 1$ km, S12 (12 m/s shear over 2.5 km) experiment (Figure 4) depicts the development of this mature circulation over the first two hours. At 40 minutes (Figure 4a), the circulation is slightly tilted downshear as the cold pool is still growing and relatively weak, and low-level convergence of air is driving updraft. By 80 minutes (Figure 4b), the system begins to tilt upright as the cold pool grows more intense. By 120 minutes (4c), an upshear tilt develops with the ascending front-to-rear flow and descending rear inflow that remain until the end of 6 hour simulation in agreement with RKW theory.

A useful metric to diagnose the convective and precipitative structure of a squall line in observations is through the radar reflectivity, Z, as it is correlated with the rate of rainfall. It is often given in a logarithmic, dBZ scale as rainfall rates span a large range of intensities. In our experiments, we use a parameterized radar reflectivity output based upon the empirical Marshall-Palmer reflectivity-rainfall model with an algorithm adopted from NOAA GFDL's FV^3-SOLO, the standalone version of FV^3. Figure 5 presents the evolution of the composite reflectivity – the maximum Z in a vertical column – and shows the self-propagation of a line of convectively-induced, intense precipitation that becomes more linearly organized by 6 hours (Figure 5c) after the short-lived precipitation

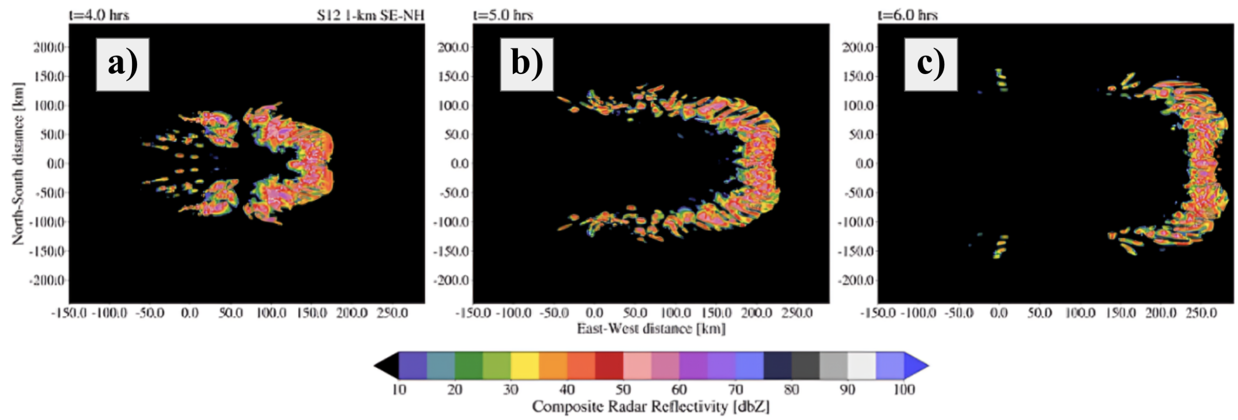

Figure 5: Composite reflectivity at 4 (a), 5 (b), and 6 (c) hours for the SE-NH $\Delta x = 1$ km experiment with 12 m/s vertical shear over the first 2.5 km above ground level (S12). A Miller cylindrical projection is used. For this projection, East-West distances correspond to physical spacing at the equator and East-West distances become stretched at higher latitudes. Distortion becomes non-negligible above/below ±100 km.

propagating against the shear dissipates. Noticeably, there is a lack of uniform, moderate stratiform precipitation trailing the region of convection. This could be caused by the simplicity of the microphysics scheme that does not model the conversion of liquid into ice and only represents liquid raindrops which have more rapid fallout speeds. Moreover, Morrison, Thompson, *et al.* 2009 found that even with the inclusion of ice microphysics, in 2D squall-line simulations with the Weather Research and Forecasting (WRF) model, bulk one-moment schemes produced negligible trailing stratiform precipitation compared to two-moment schemes.

Composite reflectivities in Figure 6 demonstrate that the experiments with 2 km and 4 km horizontal resolution produce larger, more isolated cells with more intense precipitation in alignment with simulations in the literature [Weisman, Skamarock, *et al.* 1997]. At coarser resolutions the strength of updraft is overall weaker, as expected from scaling theory. Since individual updraft cells are not yet resolved at these resolutions, it can be shown, through a Fourier-mode analysis, that the strength of buoyant updrafts should decrease at coarser horizontal resolutions [Weisman, Skamarock, *et al.* 1997].

3.2 Model Intercomparison

We consider the 1 km, S12 simulations across all three non-hydrostatic models in CESM3: MPAS, SE-NH, and FV^3. The FV^3 experiments are an outlier among the three models, so we first focus on MPAS and SE-NH. A comparison of composite reflectivity at 3 hours in Figure 7 shows that SE-NH and MPAS are relatively similar, but the MPAS simulation has more fine-scale structure and less intense precipitation. Moreover, MPAS exhibits weak precipitation trailing the primary line of convection, characteristic of stratiform precipitation. An inspection of the vertical structure of radar reflectivity and the cloud liquid content near the Equator at 4 hours in Figure 8 reveals that MPAS produces the most realistic structure among the three models. MPAS shows an anvil-shaped cloud deck with strong, convective precipitation at the leading edge and weaker convection in the

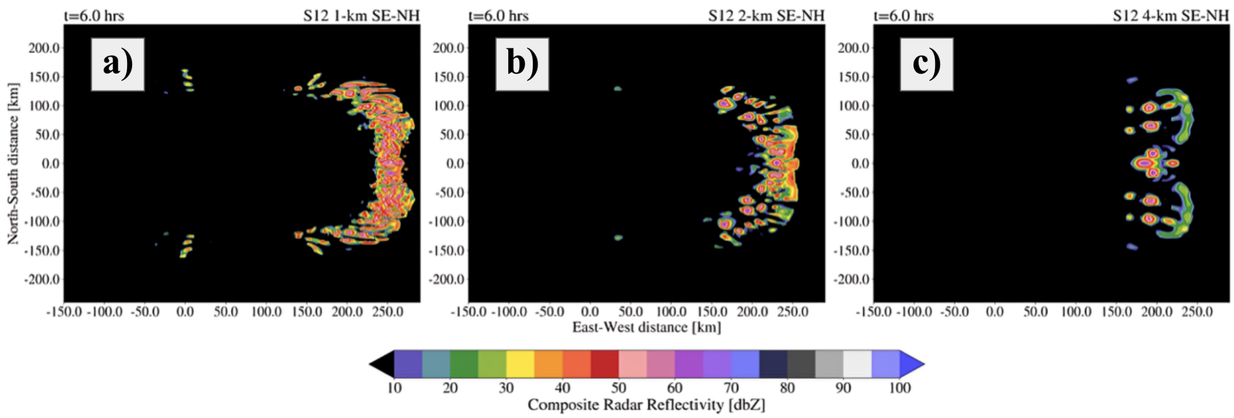

Figure 6: Composite reflectivity as in Figure 5 at 3 hours for SE-NH S12 experiments at $\Delta x = 1$ (a), 2 (b), and 4 (c) km resolutions respectively.

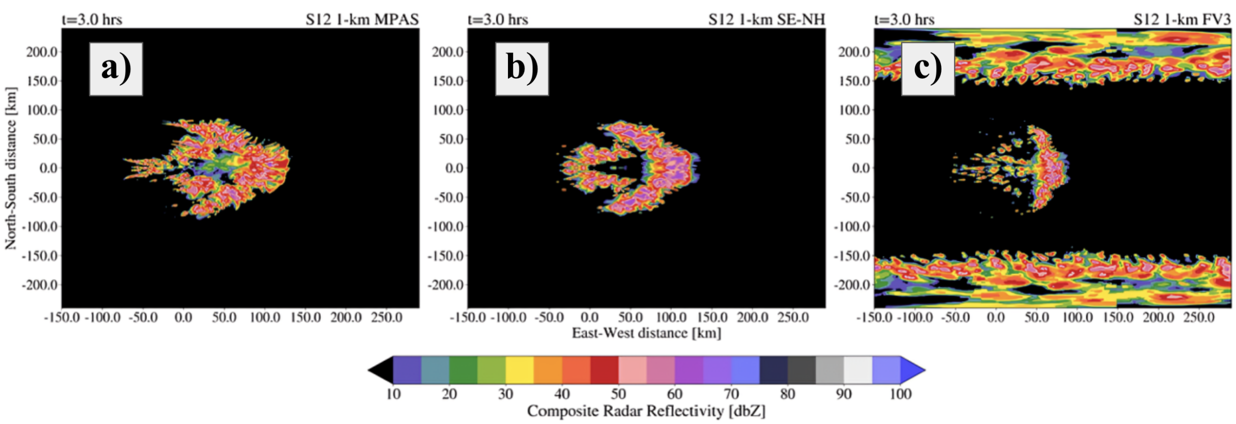

Figure 7: Composite reflectivity as in Figure 5 at 3 hours for the $\Delta x = 1$ km, S12 experiments on MPAS (a), SE-NH (b), and FV^3 (c) respectively.

older dissipating cells (Figure 8a). However, in all three models, the extent of trailing bands of stratiform precipitation are weak or non-existent. This weakness suggests that the one-moment, Kessler microphysics scheme is insufficient for capturing the stratiform features observed in squall lines. SE-NH, in particular, produces clouds only within the regions of active convection with sparse, isolated clouds in the outflow regions suggesting low residency time of cloud liquid and insufficient mixing. This demonstrates that the simplicity of the microphysics may not be the only contributing factor to simulating realistic cloud structure in these experiments.

To illustrate differences in the overall convective strength, we examine the evolution of the maximum updraft (Figure 9). Overall, the maximum updraft rapidly increases as the buoyant parcels begin to accelerate and rise in each model. MPAS and SE-NH initially peak around 20 minutes while FV^3 is slightly delayed and peaks around 40 minutes. With the most unstable CAPE, the theoretical upper limit predicted by parcel theory given by $w_{\max} = \sqrt{2 \cdot \text{CAPE}} = 70$ m/s. It is expected that updrafts ultimately fall below this limit as parcel theory does not account for the effects of entrainment, condensate loading, and contributions from vertical pressure perturbation gradients which act to reduce the buoyancy of rising parcels. Additionally, studies have shown that

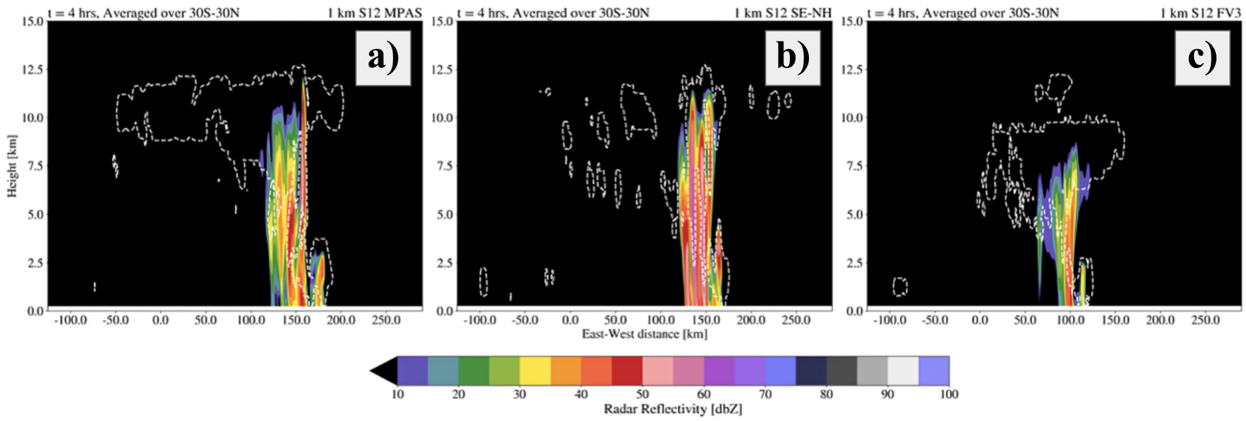

Figure 8: Vertical cross sections of the radar reflectivity (shaded) and cloud liquid moist mixing ratio (dashed contour corresponding to $q_c = 0.01$ g/kg). The radar reflectivity is the cross section at the equator and the cloud liquid field is averaged north to south across ± 30 km from the equator. Cross sections are for the $\Delta x = 1$ km, S12 experiments on MPAS (a), SE-NH (b), and FV^3 (c) respectively at 4 hours.

when convection is still underresolved, the updraft velocity scales with the effective resolution of a given simulation and increases at finer resolutions [Morrison 2016; Weisman, Skamarock, *et al.* 1997]. SE-NH, MPAS, and FV^3 achieve maximum vertical velocities as large as 66 m/s, 50 m/s, and 30 m/s respectively or about 94%, 71%, and 43% of the upper limit. Idealized squall-line simulations in Weisman & Klemp 1982 with similar instability and shear strength at 2 km grid-spacing produce updraft values around 60% of the upper limit, which will increase at a grid-spacing of 1 km. SE-NH produces particularly intense updrafts, and nearly reaches the limit, which may suggest inadequate representation of entrainment or perturbation pressure effects. The comparison of several NWPs in Bryan, Knievel, *et al.* 2006 with the same thermodynamic sounding found maximum vertical velocity in the last 3 to 6 hours to lie between $36\% - 55\%$ of the theoretical limit for vertical shear strengths between $10 - 15$ m/s. MPAS, FV^3, and SE-NH show 51%, 59%, and 20% respectively. In fact, across shear strengths between $0 - 40$ m/s, no model produced a maximum updraft below 20 m/s [Bryan, Knievel, *et al.* 2006].

FV^3 is an outlier among the models. The simulations produce artificial precipitation features near both poles that begin to propagate toward the Equator and disrupt the squall line produced by the initial perturbation trigger after 3 hours. It remains unclear what causes this instability. At coarser resolutions, these features at the poles do not appear. An analysis of the vertical structure (Figure 8) and updraft strength (Figure 9) also demonstrate that the convective updraft and precipitation features are relatively weak and shallow. These results are in stark contrast to the literature of squall line simulations with the FV^3 model. Recent work from Lou Wicker simulated squall lines with FV^3-SOLO on a regional, flat domain using the same shear strength and initial CAPE. They did not observe numerical instabilities, but instead updrafts that were excessively strong compared to another non-hydrostatic NWP model, CM1. Motivated by these simulations, we ran an additional simulation with FV^3 using the same diffusion settings as Wicker, based on the minimally diffusive settings of RRFS. The composite reflectivity (Figure 10) still exhibits the poleward instability and additionally produces gridpoint storms at the corners of the cubed-sphere grid – where the grid areas

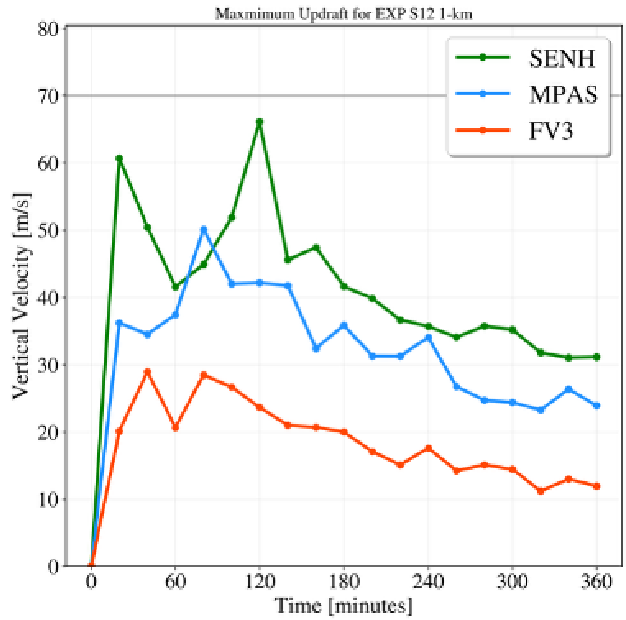

Figure 9: Comparisons of the evolution in maximum updraft strength across the $\Delta x = 1$ km, S12 experiments with MPAS, SE-NH, and FV^3. The gray horizontal line at 70 m/s in the updraft evolution corresponds to the theoretical maximum updraft based on parcel theory using the CAPE of the most unstable parcel path.

are smallest. The squall line updraft strength and precipitation remain weak compared to SE-NH and MPAS but has a larger horizontal extent with more intense precipitation than the original FV^3 simulation. Note, however, that Wicker's simulations differ in a few ways. While these simulations use the cylinder perturbation, Wicker uses 5 bubbles separated by 30 km. Additionally, these simulations are run on a cubed-sphere over a spherical domain compared with the flat, Cartesian plane used by Wicker. Moreover, the FV^3 coupling with CAM differs from FV^3-SOLO's coupling with physics. In particular, FV^3-CAM calls physics and then dynamics when updating a state, whereas FV^3-SOLO calls dynamics first. These do not necessarily give the same results and at coarse enough time steps may become relevant [Gross *et al.* 2018].

4 Conclusion

The proof-of-concept study of squall line structure in the reduced-radius framework from Klemp, Skamarock & Park 2015 provides a computationally efficient method to benchmark the dynamical representation of organized convection in global storm-resolving models. The results of SE-NH simulations demonstrate that the essential dynamical circulations within the squall line are well captured at $\Delta x = 1$ km without a subgrid turbulence closure and with only a simple one-moment microphysics scheme of liquid water processes. In accordance with RKW theory, the squall line transitions from a downshear tilt to the mature, upshear tilted circulation developing characteristic features such as the gust front, rear inflow, and the front-to-rear ascending flow that drives new convection above the propagating cold pool. However, in comparison to MPAS, SE-NH produces a system with more intense updrafts and precipitation along with a poor representation of anvil cloud

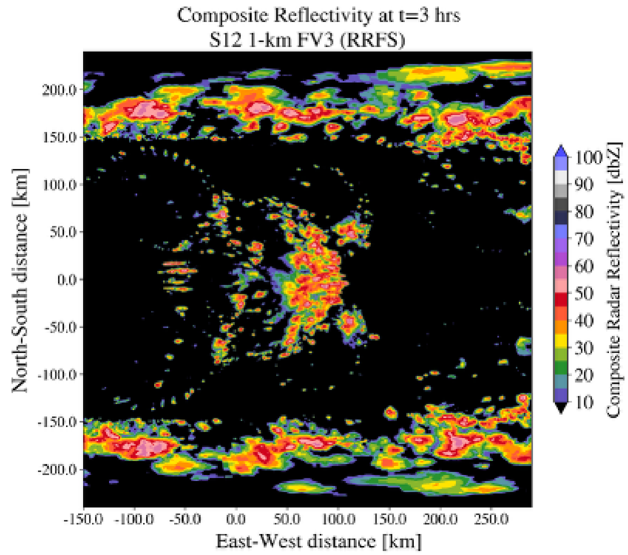

Figure 10: Composite reflectivity as in Figure 5 at 3 hours for the $\Delta x = 1$ km, S12 experiments for FV^3 with a RRFS diffusion configuration.

structure and trailing stratiform precipitation. Whether this is caused by a difference in the numerical schemes of the dynamical core or due to the lack of turbulence closure within SE-NH remains unclear. To determine whether these results are robust, future work will incorporate the full suite of CAM7 physics, which include schemes like a two-moment microphysics that includes ice phases (PUMAS; Gettelman *et al.* 2023) and a planetary boundary layer scheme that parameterizes subgrid momentum fluxes (CLUBB; Golaz *et al.* 2002). Moist thermal experiments used in studies like Bryan & Fritsch 2002 and Morrison 2016 suggest another avenue to benchmark the representation of vertical pressure perturbation and entrainment effects on buoyancy within a simpler, shearless environment. These experiments could be easily adapted to the reduced-radius framework.

The analysis for the intercomparison presented in this study focused primarily on qualitative comparisons of the horizontal and vertical structure. This reveals clear differences across each model. To attribute model sensitivities to their treatment of numerical and physical mixing, we plan to explore kinetic energy spectra, a common technique used to quantify the effect of diffusion and to measure the effective resolution of models [Skamarock 2004]. At the gray-zone, the effective resolution ultimately determines the smallest scales of convection that can be represented [Prein, Wang, *et al.* 2025]. Additionally, the recent work of Wicker 2026 (in review) displays how intermodel differences in squall line evolution can be sensitive to the environmental background of the squall line, in particular the shear strength and the amount of CAPE instability. Moreover, the simulations within this study focus on squall lines in the midlatitudes which differ, characteristically, from tropical squall lines. Tropical MCSs are characterized by abundant moisture, weak shear, and CAPE profiles that are narrow and deep (compared to midlatitude CAPE profiles) [Prein, Wang, *et al.* 2025]. It is important to explore this parameter space to further understand convective sensitivities across the global domain to the choice of dynamical core.

Finally, the unusual results of the FV^3 simulations raises important questions about the efficacy of the reduced-radius framework and the sensitivity of convection to physics-dynamics coupling. The FV^3 implementation in CAM is neither well supported nor tested compared to SE-NH and

MPAS. Applying the same initialization procedure used in this study to FV^3-SOLO on a flat Cartesian plane and in the reduced-radius framework, could identify whether the results are isolated to the FV^3-CAM implementation or due to the spherical, reduced-radius domain. Furthermore, the FV^3 physics-dynamics coupling in CAM uses a sequential update splitting approach that acts as a hard adjustment rather than the dribbling scheme applied in SE-NH and MPAS. Experiments with physics and dynamics without any subcycling, so that dynamics and physics are run at the same time step, can provide a tool to remove the model differences due to physics-dynamics coupling approaches.

References

1. Ban, N., Schmidli, J. & Schär, C. Evaluation of the convection-resolving regional climate modeling approach in decade-long simulations. *Journal of Geophysical Research: Atmospheres* **119,** 7889–7907. doi:10.1002/2014JD021478 (2014).
2. Bannon, P. R. Hydrostatic Adjustment: Lamb's Problem. *Journal of the Atmospheric Sciences* **52,** 1743–1752. doi:10.1175/1520-0469(1995)052<1743:HALP>2.0.CO;2 (1995).
3. Berthou, S. *et al.* Pan-European climate at convection-permitting scale: a model intercomparison study. *Climate Dynamics* **55,** 35–59. doi:10.1007/s00382-018-4114-6 (2020).
4. Bryan, G. H. & Fritsch, J. M. A Benchmark Simulation for Moist Nonhydrostatic Numerical Models. EN. *Monthly Weather Review* **130,** 2917–2928. doi:10.1175/1520-0493(2002)130<2917:ABSFMN>2.0.CO;2 (Dec. 2002).
5. Bryan, G. H., Knievel, J. C. & Parker, M. D. A Multimodel Assessment of RKW Theory's Relevance to Squall-Line Characteristics. *Monthly Weather Review* **134,** 2772–2792. doi:10.1175/MWR3226.1 (2006).
6. Bryan, G. H. & Morrison, H. Sensitivity of a Simulated Squall Line to Horizontal Resolution and Parameterization of Microphysics. *Monthly Weather Review.* doi:10.1175/MWR-D-11-00046.1 (2012).
7. Bryan, G. H., Wyngaard, J. C. & Fritsch, J. M. Resolution Requirements for the Simulation of Deep Moist Convection. *Monthly Weather Review* (2003).
8. Caldwell, P. M. *et al.* Convection-Permitting Simulations With the E3SM Global Atmosphere Model. *Journal of Advances in Modeling Earth Systems* **13,** e2021MS002544. doi:10.1029/2021MS002544 (2021).
9. Ceppi, P., Brient, F., Zelinka, M. D. & Hartmann, D. L. Cloud feedback mechanisms and their representation in global climate models. *WIREs Climate Change* **8,** e465. doi:10.1002/wcc.465 (2017).
10. Chen, D. *et al.* in *Climate Change 2021: The Physical Science Basis. Contribution of Working Group I to the Sixth Assessment Report of the Intergovernmental Panel on Climate Change* (eds Masson-Delmotte, V. *et al.*) 147–286 (Cambridge University Press, Cambridge, UK and New York, NY, USA, 2021). doi:10.1017/9781009157896.003.

11. Dennis, J. *et al.* High-Resolution Mesh Convergence Properties and Parallel Efficiency of a Spectral Element Atmospheric Dynamical Core. *The International Journal of High Performance Computing Applications* **19,** 225–235. doi:10.1177/1094342005056108 (2005).

12. Dennis, J. M. *et al.* CAM-SE: A scalable spectral element dynamical core for the Community Atmosphere Model. *The International Journal of High Performance Computing Applications* **26,** 74–89. doi:10.1177/1094342011428142 (2012).

13. Donahue, A. S., Caldwell, P. M., *et al.* To Exascale and Beyond—The Simple Cloud-Resolving E3SM Atmosphere Model (SCREAM), a Performance Portable Global Atmosphere Model for Cloud-Resolving Scales. *Journal of Advances in Modeling Earth Systems* **16,** e2024MS004314. doi:10.1029/2024MS004314 (2024).

14. Donahue, A. S. & Caldwell, P. M. Impact of Physics Parameterization Ordering in a Global Atmosphere Model. *Journal of Advances in Modeling Earth Systems* **10,** 481–499. doi:10.1002/2017MS001067 (2018).

15. Donahue, A. S. & Caldwell, P. M. Performance and Accuracy Implications of Parallel Split Physics-Dynamics Coupling in the Energy Exascale Earth System Atmosphere Model. *Journal of Advances in Modeling Earth Systems* **12,** e2020MS002080. doi:10.1029/2020MS002080 (2020).

16. Feng, Z. *et al.* Mesoscale Convective Systems in DYAMOND Global Convection-Permitting Simulations. *Geophysical Research Letters* **50,** e2022GL102603. doi:10.1029/2022GL102603 (2023).

17. Freischem, L. J., Weiss, P., Christensen, H. M. & Stier, P. Multifractal Analysis for Evaluating the Representation of Clouds in Global Kilometer-Scale Models. *Geophysical Research Letters* **51,** e2024GL110124. doi:10.1029/2024GL110124 (2024).

18. Gettelman, A. *et al.* Importance of ice nucleation and precipitation on climate with the Parameterization of Unified Microphysics Across Scales version 1 (PUMASv1). English. *Geoscientific Model Development* **16,** 1735–1754. doi:10.5194/gmd-16-1735-2023 (Mar. 2023).

19. Golaz, J.-C., Larson, V. E. & Cotton, W. R. A PDF-Based Model for Boundary Layer Clouds. Part I: Method and Model Description. EN. *Journal of the Atmospheric Sciences* **59,** 3540–3551. doi:10.1175/1520-0469(2002)059<3540:APBMFB>2.0.CO;2 (Dec. 2002).

20. Gross, M. *et al.* Physics–Dynamics Coupling in Weather, Climate, and Earth System Models: Challenges and Recent Progress. *Monthly Weather Review* **146,** 3505–3544. doi:10.1175/MWR-D-17-0345.1 (2018).

21. Haberlie, A. M. & Ashley, W. S. A Radar-Based Climatology of Mesoscale Convective Systems in the United States. doi:10.1175/JCLI-D-18-0559.1 (2019).

22. Houze Jr., R. A. Mesoscale convective systems. *Reviews of Geophysics* **42.** doi:10.1029/2004RG000150 (2004).

23. Kendon, E. J., Roberts, N. M., Senior, C. A. & Roberts, M. J. Realism of Rainfall in a Very High-Resolution Regional Climate Model. *Journal of Climate* **25,** 5791–5806. doi:10.1175/JCLI-D-11-00562.1 (2012).

24. Klemp, J. B., Skamarock, W. C. & Dudhia, J. Conservative Split-Explicit Time Integration Methods for the Compressible Nonhydrostatic Equations. *Monthly Weather Review* **135,** 2897–2913. doi:10.1175/MWR3440.1 (2007).

25. Klemp, J. B., Skamarock, W. C. & Park, S.-H. Idealized global nonhydrostatic atmospheric test cases on a reduced-radius sphere. *Journal of Advances in Modeling Earth Systems* **7,** 1155–1177. doi:10.1002/2015MS000435 (2015).

26. Klemp, J. B. & Wilhelmson, R. B. Simulations of Right- and Left-Moving Storms Produced Through Storm Splitting. EN. *Journal of the Atmospheric Sciences* **35,** 1097–1110. doi:10.1175/1520-0469(1978)035<1097:SORALM>2.0.CO;2 (June 1978).

27. Klemp, J. B. & Wilhelmson, R. B. The Simulation of Three-Dimensional Convective Storm Dynamics. *Journal of the Atmospheric Sciences* **35,** 1070–1096. doi:10.1175/1520-0469(1978)035<1070:TSOTDC>2.0.CO;2 (1978).

28. Lai, K. T. & Waite, M. L. Resolution Dependence and Subfilter-Scale Motions in Idealized Squall-Line Simulations. *Monthly Weather Review* **148,** 3059–3078. doi:10.1175/MWR-D-19-0330.1 (2020).

29. Lawrence, B. N. *et al.* Crossing the chasm: how to develop weather and climate models for next generation computers? *Geoscientific Model Development* **11,** 1799–1821. doi:10.5194/gmd-11-1799-2018 (2018).

30. Lebo, Z. J. & Morrison, H. Effects of Horizontal and Vertical Grid Spacing on Mixing in Simulated Squall Lines and Implications for Convective Strength and Structure. *Monthly Weather Review* **143,** 4355–4375. doi:10.1175/MWR-D-15-0154.1 (2015).

31. Lin, S.-J. A "vertically Lagrangian" finite-volume dynamical core for global models. *Mon. Wea. Rev.* **132,** 2293–2307 (2004).

32. Moeng, C.-H., Sullivan, P. P., Khairoutdinov, M. F. & Randall, D. A. A Mixed Scheme for Subgrid-Scale Fluxes in Cloud-Resolving Models. *Journal of the Atmospheric Sciences* **67,** 3692–3705. doi:10.1175/2010JAS3565.1 (2010).

33. Morrison, H., Thompson, G. & Tatarskii, V. Impact of Cloud Microphysics on the Development of Trailing Stratiform Precipitation in a Simulated Squall Line: Comparison of One- and Two-Moment Schemes. *Monthly Weather Review* **137,** 991–1007. doi:10.1175/2008MWR2556.1 (2009).

34. Morrison, H. Impacts of Updraft Size and Dimensionality on the Perturbation Pressure and Vertical Velocity in Cumulus Convection. Part II: Comparison of Theoretical and Numerical Solutions and Fully Dynamical Simulations. EN. *Journal of the Atmospheric Sciences* **73,** 1455–1480. doi:10.1175/JAS-D-15-0041.1 (Apr. 2016).

35. Morrison, H., Morales, A. & Villanueva-Birriel, C. Concurrent Sensitivities of an Idealized Deep Convective Storm to Parameterization of Microphysics, Horizontal Grid Resolution, and Environmental Static Stability. *Monthly Weather Review* **143,** 2082–2104. doi:10.1175/MWR-D-14-00271.1 (2015).

36. Potvin, C. K. & Flora, M. L. Sensitivity of Idealized Supercell Simulations to Horizontal Grid Spacing: Implications for Warn-on-Forecast. *Monthly Weather Review* **143,** 2998–3024. doi:10.1175/MWR-D-14-00416.1 (2015).

37. Prein, A. F., Langhans, W., *et al.* A review on regional convection-permitting climate modeling: Demonstrations, prospects, and challenges. *Reviews of Geophysics* **53,** 323–361. doi:10.1002/2014RG000475 (2015).
38. Prein, A. F., Wang, D., Ge, M., Ramos Valle, A. & Chasteen, M. B. Resolving Mesoscale Convective Systems: Grid Spacing Sensitivity in the Tropics and Midlatitudes. *Journal of Geophysical Research: Atmospheres* **130,** e2024JD042530. doi:10.1029/2024JD042530 (2025).
39. Putman, W. M. & Lin, S.-J. Finite-volume transport on various cubed-sphere grids. *J. Comput. Phys.* **227,** 55–78 (2007).
40. Ringler, T., Thuburn, J., Klemp, J. & Skamarock, W. A unified approach to energy conservation and potential vorticity dynamics for arbitrarily-structured C-grids. *Journal of Computational Physics* **229,** 3065–3090. doi:10.1016/j.jcp.2009.12.007 (2010).
41. Satoh, M. *et al.* Global Cloud-Resolving Models. *Current Climate Change Reports* **5,** 172–184. doi:10.1007/s40641-019-00131-0 (2019).
42. Scafetta, N. Advanced Testing of Low, Medium, and High ECS CMIP6 GCM Simulations Versus ERA5-T2m. *Geophysical Research Letters* **49,** e2022GL097716. doi:10.1029/2022GL097716 (2022).
43. Schär, C. *et al.* Kilometer-Scale Climate Models: Prospects and Challenges. *Bulletin of the American Meteorological Society* **101,** E567–E587. doi:10.1175/BAMS-D-18-0167.1 (2020).
44. Skamarock, W. C. Evaluating Mesoscale NWP Models Using Kinetic Energy Spectra. EN. *Monthly Weather Review* **132,** 3019–3032. doi:10.1175/MWR2830.1 (Dec. 2004).
45. Skamarock, W. C. *et al.* A Multiscale Nonhydrostatic Atmospheric Model Using Centroidal Voronoi Tesselations and C-Grid Staggering. *Monthly Weather Review* **140,** 3090–3105. doi:10.1175/MWR-D-11-00215.1 (2012).
46. Smagorinsky, J. General Circulation Experiments with the Primitive Equations: I. The Basic Experiment. *Monthly Weather Review* **91,** 99–164. doi:10.1175/1520-0493(1963)091<0099:GCEWTP>2.3.CO;2 (1963).
47. Stevens, B. *et al.* DYAMOND: the DYnamics of the Atmospheric general circulation Modeled On Non-hydrostatic Domains. *Progress in Earth and Planetary Science* **6,** 61. doi:10.1186/s40645-019-0304-z (2019).
48. Takemi, T. & Rotunno, R. The Effects of Subgrid Model Mixing and Numerical Filtering in Simulations of Mesoscale Cloud Systems. *Monthly Weather Review* **131,** 2085–2101. doi:10.1175/1520-0493(2003)131<2085:TEOSMM>2.0.CO;2 (2003).
49. Taylor, M. A. *et al.* An Energy Consistent Discretization of the Nonhydrostatic Equations in Primitive Variables. *Journal of Advances in Modeling Earth Systems* **12.** doi:10.1029/2019MS001783 (2020).
50. Thuburn, J., Ringler, T., Skamarock, W. & Klemp, J. Numerical representation of geostrophic modes on arbitrarily structured C-grids. *Journal of Computational Physics* **228,** 8321–8335. doi:10.1016/j.jcp.2009.08.006 (2009).

51. Ullrich, P. A. *et al.* DCMIP2016: a review of non-hydrostatic dynamical core design and intercomparison of participating models. *Geoscientific Model Development* **10,** 4477–4509. doi:10.5194/gmd-10-4477-2017 (2017).

52. Weisman, M. L. & Klemp, J. B. The Dependence of Numerically Simulated Convective Storms on Vertical Wind Shear and Buoyancy. *Monthly Weather Review* **110,** 504–520. doi:10.1175/1520-0493(1982)110<0504:TDONSC>2.0.CO;2 (1982).

53. Weisman, M. L. & Rotunno, R. "A Theory for Strong Long-Lived Squall Lines" Revisited. *Journal of the Atmospheric Sciences* (2004).

54. Weisman, M. L., Skamarock, W. C. & Klemp, J. B. The Resolution Dependence of Explicitly Modeled Convective Systems. *Monthly Weather Review* (Apr. 1, 1997).

55. Wyngaard, J. C. Toward Numerical Modeling in the "Terra Incognita". *Journal of the Atmospheric Sciences* **61,** 1816–1826. doi:10.1175/1520-0469(2004)061<1816:TNMITT>2.0.CO;2 (2004).

56. Zarzycki, C. M. *et al.* DCMIP2016: the splitting supercell test case. *Geoscientific Model Development* **12,** 879–892. doi:10.5194/gmd-12-879-2019 (2019).

57. Zhang, C. Madden-Julian Oscillation. *Reviews of Geophysics* **43.** doi:10.1029/2004RG000158 (2005).

58. Zhang, K. *et al.* Impact of numerical choices on water conservation in the E3SM Atmosphere Model version 1 (EAMv1). *Geoscientific Model Development* **11,** 1971–1988. doi:10.5194/gmd-11-1971-2018 (2018).